ADVANCED FUNCTIONAL MATERIALS
www.afm-journal.de

Nanoarchitectonics-Enabled Stimulus-Selective Energetics: Nacre-Mimetic Interfaces Synchronize Structural Resilience and Enhanced Energy Release

*Jingwei Li, Zhichao Zhao, Yihao Shen, Yongsheng Jia, Jinshan Sun, Yingkang Yao, Quanmin Xie, Yurong Liu, Guangyu Yin, Zhangbo Ming, and Xuwen Liu**

The practical application of Metastable Intermolecular Composites (MICs) has long been constrained by an intrinsic trade-off: the high specific surface area required for rapid energy release inevitably induces extreme sensitivity and structural fragility, while conventional stabilizing additives compromise energy density. To resolve this, we present a bio-inspired geometric-interfacial nanoarchitectural strategy. Hierarchically ordered films were engineered via the oriented assembly of 2D flake aluminum (F-Al) and flake copper oxide (F-CuO) into a nacre-mimetic "brick-and-mortar" architecture. This design enhances stimulus-specific response: edge stress concentration in F-Al reduces thermal ignition thresholds by >40%, while percolating conductive networks increase electrostatic safety by 73%. Mechanically, the architecture improves strength and toughness by >300% through crack deflection and frictional dissipation. Furthermore, energy release efficiency is amplified, achieving an 8-fold increase in flame propagation (128 mm s^{-1}) driven by anisotropic thermal conduction and fluorine-mediated interface activation. This work establishes geometric-interfacial nanoarchitectonics as a paradigm to synchronize stress, charge, and heat transport, enabling next-generation energetic materials for aerospace and Micro-Electromechanical Systems (MEMS).

1. Introduction

Metastable Intermolecular Composites (MICs) have garnered significant research interest in recent years, owing to their substantially higher energy density, faster energy release rate, and tunable reaction characteristics compared to traditional molecular energetic materials (e.g., TNT, RDX).[1–5] Typical MICs systems consist of nano/microscale metallic fuels combined with metal oxide oxidizers. Their energy release originates from violent redox reactions between the components.[6–8] This unique reaction mechanism endows MICs with immense potential for miniaturized, high-precision applications, such as micropropulsion systems, miniature detonation devices, and Micro-Electromechanical System (MEMS) igniters.[8–10]

However, the practical engineering application of MICs faces long-standing critical challenges. On the one hand, the high proportion of nano-active components or the intentionally designed high porosity often results in a structurally loose material with weak cohesion.[11,12] This significantly compromises its mechanical strength and toughness, rendering it unable to withstand the mechanical demands of complex application environments, such as aircraft vibrations and impact loads.[11,12] On the other hand, the enormous specific surface area and surface energy of nano-active components make them exceptionally sensitive to external stimuli like electrostatic discharge, friction, and thermal shock, posing serious safety hazards.[13,14] The triggering spark energy for certain unoptimized MICs systems can be as low as 0.1 mJ,[15–17] far below the electrostatic energy typically carried by a human body. Moreover, and critically, strategies designed to mitigate electrostatic sensitivity or enhance mechanical integrity invariably compromise energy release characteristics. For instance, introducing inert binders can improve mechanical integrity and reduce certain sensitivities, but it dilutes the active components, lowering energy density and reaction rate.[13] Coating or passivating particles can effectively reduce sensitivity, but it may also hinder intimate contact between fuel and oxidizer, similarly increasing ignition delay.[18] Therefore, developing a new construction strategy that can synergistically optimize sensitivity, mechanical strength, and energy release efficiency has become an important challenge for MICs toward practical applications.

In recent years, the 2D design of energy materials has provided new ideas for solving the coordinated optimization of mechanical properties and functionality.[19,20] A prime example is the nacre-mimetic "brick-and-mortar" hierarchical structure, characterized by the ordered arrangement of 2D lamellar components.[21,22] This architecture effectively overcomes the inherent brittleness

J. Li, Z. Zhao, Y. Shen, Y. Jia, J. Sun, Y. Yao, Q. Xie, Y. Liu, G. Yin, Z. Ming, X. Liu
State Key Laboratory of Precision Blasting
Jianghan University
Wuhan 430113, China
E-mail: lxw@jhun.edu.cn
J. Li, Y. Jia, J. Sun, Y. Yao, Q. Xie, Y. Liu, X. Liu
Hubei Key Laboratory of Blasting Engineering
Jianghan University
Wuhan 430056, China

The ORCID identification number(s) for the author(s) of this article can be found under https://doi.org/10.1002/adfm.202525995

DOI: 10.1002/adfm.202525995

of its constituent phases through various toughening mechanisms, such as crack deflection, interlayer sliding, and organic phase bridging, thereby achieving a remarkable synergy between strength and toughness.[21–25] While various biological hierarchies, including the columnar structure of tooth enamel and the fibrous networks of bone, each provide distinct advantages in mechanical resilience and adaptability,[26,27] the nacre-mimetic architecture offers particular benefits for MICs through its emphasis on extensive face-to-face interfacial contacts between components.[28–30] Introducing this 2D construction strategy into MICs system design holds significant potential. The interlocking effect between lamellae could substantially enhance the mechanical properties of traditional composite energetic systems. Concurrently, leveraging the anisotropic regulation of electrostatic and thermal transport inherent to 2D topological structures offers a pathway for the active control of external stimulus response. Pioneering research[31,32] has provided initial evidence for the performance advantages of 2D architectures in energetic systems. Therefore, it is necessary to conduct more in-depth studies on this strategy, focusing on its overall impact on energetic systems and elucidating the underlying mechanisms leading to the observed phenomena.

To resolve the fundamental trade-offs among mechanical integrity, safety, and energy release efficiency that have long constrained MICs, we herein propose a bioinspired nanoarchitectonic strategy. Distinct from recent advancements[33–35] that utilize vacuum-assisted filtration primarily for inert fillers or single-component 2D phases, this work pioneers the construction of a "double-2D" reactive architecture by integrating two-dimensionally transformed flake CuO (F-CuO) as an active "brick" component with flake Al (F-Al). Engineered via mechanical ball milling and evaporation-induced self-assembly, this nacre-mimetic design exploits the geometric matching of high-aspect-ratio components to establish continuous "face-to-face" reactive interfaces. Systematic investigations encompass microstructural evolution, interfacial chemistry, mechanical response under stress, stimulus-selective sensitivity (thermal/electrostatic), combustion dynamics, and PIR pathways. By correlating architectural features with emergent properties, we elucidate the mechanistic basis of the synergistic "mechanical strengthening–energy release optimization–sensitivity passivation" triad inherent to the 2D-MIC system. These findings establish geometric-interfacial nanoarchitectonics as a paradigm for synchronizing traditionally antagonistic properties in energetic materials, providing foundational principles for next-generation high-safety, structurally resilient smart energetics.

2. Results and Discussion

2.1. Morphology

High-energy ball milling—a representative mechanical alloying technique—was successfully used to transform aluminum powder from spherical particles (S-Al) to 2D flake structures (F-Al). Scanning electron microscopy (SEM) and high-resolution transmission electron microscopy (HRTEM) characterization revealed that pristine S-Al particles exhibited regular spherical morphology (**Figure 1**a–c) with a median particle diameter (D_{50}) of 4.8 µm (Figure S5, Supporting Information). Ball milling induced significant plastic deformation and cold welding, resulting in lateral expansion of F-Al to 50–300 µm (Figure 1d–f; Figure S6, Supporting Information) with high aspect ratios. This 2D morphological transition substantially increased the fuel's specific surface area, providing abundant active sites for fuel/oxidizer interfacial reactions (Figure 1g).

HRTEM with selected area electron diffraction (SAED) analysis further demonstrated that ball milling reconstructed both surface oxide layers and crystalline structure. While S-Al featured a smooth, homogeneous amorphous oxide layer (Figure 1c,h), ball-milled F-Al developed a rough, heterogeneous oxide layer (Figure 1f,h). Thickness profiling across representative regions (Figure 1h,i) quantified this evolution. S-Al exhibited uniform oxide thickness (variance: 0.015), whereas F-Al showed significant thickness fluctuations (variance: 0.552). This pronounced thickness heterogeneity is not accidental but originates from the "dynamic fracture-repassivation" cycles inherent to the high-energy ball milling process.[36,37] The intense mechanical impact drives continuous plastic deformation and cold welding, which prevents the growth of a uniform oxide layer. Unlike the smooth, homogeneous shell of S-Al, this structurally irregular oxide layer introduces abundant microscopic defects and high-aspect-ratio features. These morphological fluctuations are instrumental in modulating the material's physicochemical properties, serving as the structural basis for the enhanced performance discussed in subsequent sections.

SAED patterns provided further insight into the crystallographic changes induced by ball milling. The S-Al exhibited sharp diffraction spots (Figure 1c), indicating well-defined single-crystalline characteristics. In contrast, the F-Al displayed diffuse diffraction rings superimposed with spotty patterns (Figure 1f), suggesting partial amorphization and polycrystallinity. This structural transition was corroborated by X-ray diffraction (XRD) analysis (Figure 1j). Both samples showed characteristic Al diffraction peaks (JCPDS #85-1327) at 2θ = 38.5° (111), 44.7° (200), 65.1° (220), and 78.2° (311). However, significant peak broadening was observed in F-Al, with the full width at half maximum (FWHM) of the (111) peak increasing from 0.09° (S-Al) to 0.21° (Figure 1j). This pronounced broadening confirms lattice distortion and grain refinement resulting from intense mechanical deformation during ball milling.

Following comprehensive characterization of individual 2D components, composite films were fabricated to validate the scalability of 2D architectural strategy. Free-standing energetic films with "brick-and-mortar" hierarchy were constructed via vacuum-assisted filtration self-assembly (**Figure 2**a), employing 2D F-Al and F-CuO as rigid bricks bonded by a fluoropolymer mortar phase. The vacuum-induced planar orientation effect enabled multiscale ordered assembly, yielding mechanically robust films with macroscopic structural integrity. Remarkably, these films exhibited exceptional flexibility, permitting bending, folding, and twisting without fracture (Figure 2b). The selection of the nacre-mimetic structure is further justified by its synthesis compatibility with energetic materials. The nacre-like "brick" units are efficiently generated via the top-down mechanical ball milling of commercial spherical powders. This process exploits the plastic deformation of aluminum to form high-aspect-ratio platelets, which naturally self-assemble into ordered layered structures via vacuum filtration to minimize system surface energy. This route

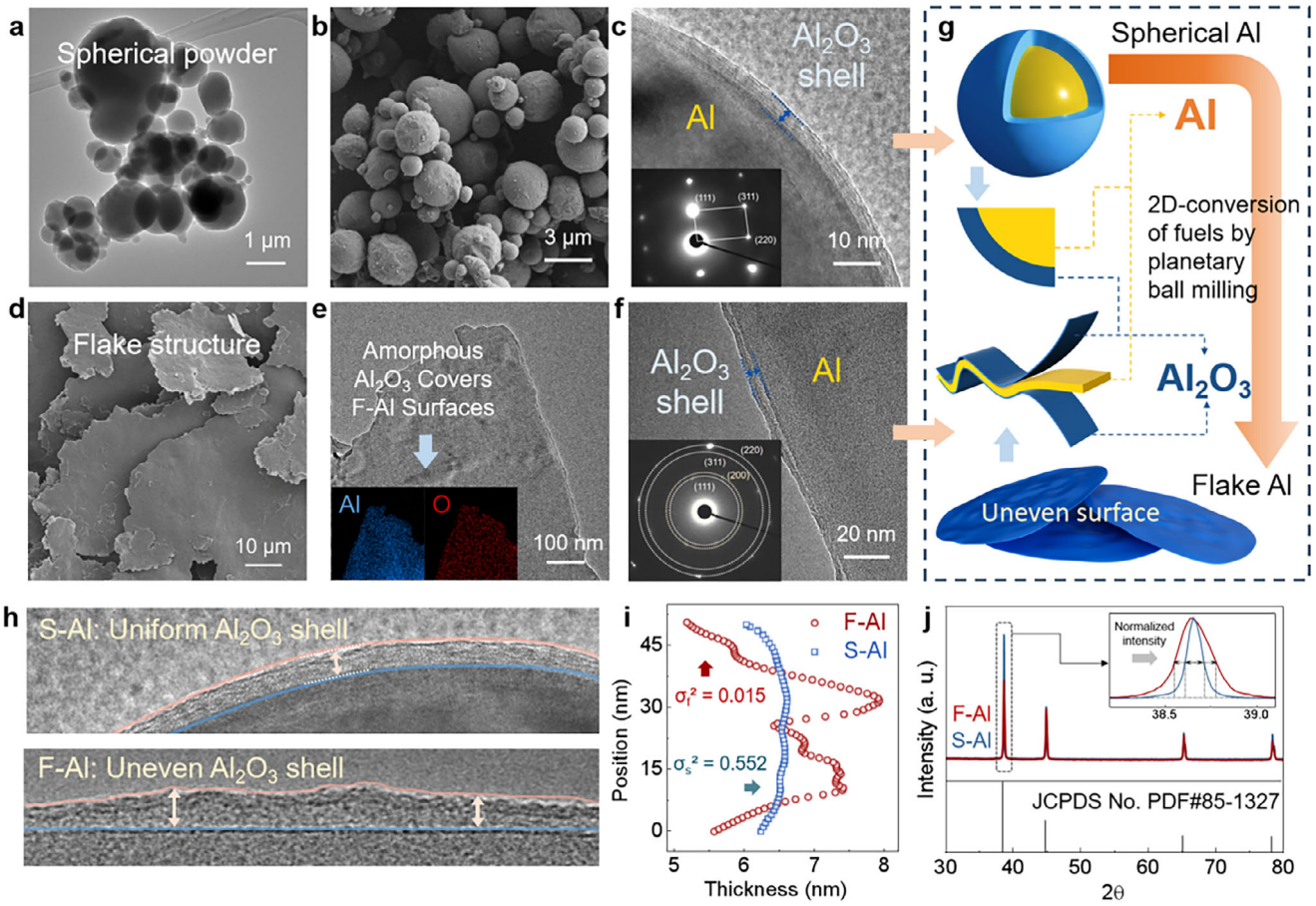

Figure 1. Morphology and interface characteristics of F-Al/S-Al powder. SEM, HRTEM and SEAD characterization of a–c) S-Al and d–f) F-Al. g) Schematic diagram of the 2D transformation. h) Structural characteristics of the Al_2O_3 interface layer and i) regional thickness analysis. j) XRD spectra of S-Al and F-Al.

avoids the use of extensive inert templates or complex scaffolds often required for other bio-inspired geometries, ensuring that the high energy density of the MICs is preserved while achieving structural coherence.

Cross-sectional SEM analysis (Figure 2c,d) revealed a well-defined lamellar architecture with alternating F-Al and F-CuO platelets bonded by fluoropolymer interlayers. Both components exhibited pronounced in-plane alignment, confirming vacuum-induced preferential orientation during filtration. Surface SEM imaging (Figure 2e,f) demonstrated tight geometric interlocking between platelets, indicating uniform interfacial integration. HRTEM-EDS analysis (Figure 2g,h) elucidated interfacial bonding characteristics, where spatial correlation of F and Al signals confirmed fluoropolymer coating on aluminum surfaces. While HRTEM-EDS confirms the spatial distribution of elements, the specific molecular interactions at the interface were further elucidated via FT-IR analysis (Figure S8, Supporting Information). The spectra reveal a distinct blue shift in the C-F stretching vibration peaks within the 1000–1100 cm^{-1}. This shift is attributed to the formation of hydrogen bonds (O-H···F) between the residual surface hydroxyl groups on the Al_2O_3/CuO shells and the fluorine atoms in the Viton matrix. Critically, CuO layers bridge to Al through continuous polymer linkages, establishing an integrated interfacial network (Figure 2h). This interlayered structure helps to enhance the mechanical properties of the film.[28,38] To quantitatively evaluate the mechanical properties of the nacre-inspired energetic architecture, tensile testing was performed using a universal testing machine (Figure 2i). The stress-strain curves revealed that the composite system incorporating F-Al and F-CuO exhibited superior tensile performance (Figure 2j). Specifically, ACF-FF (Al/CuO/fluoropolymer films composed of F-Al and F-CuO; see experimental section for detailed nomenclature) achieved the highest tensile strength (5.35 MPa) and toughness (0.227 MJ m^{-3}), confirming that the nacre-like structural design significantly improved the mechanical properties.

Enhanced mechanical properties primarily originate from the synergistic hard/soft phase interaction and high interlayer friction within the nacre-like architecture.[21,39] The rigid F-Al and F-CuO phases provide high strength, while the compliant Viton binder enables substantial deformation capacity. Under stress, these phases undergo cooperative deformation, effectively mitigating stress concentration that would otherwise trigger brittle fracture. This synergistic interaction simultaneously elevates both strength and toughness.[21,39] Furthermore, the high frictional resistance between adjacent lamellae (F-Al/F-CuO) dissipates significant energy through controlled interlayer

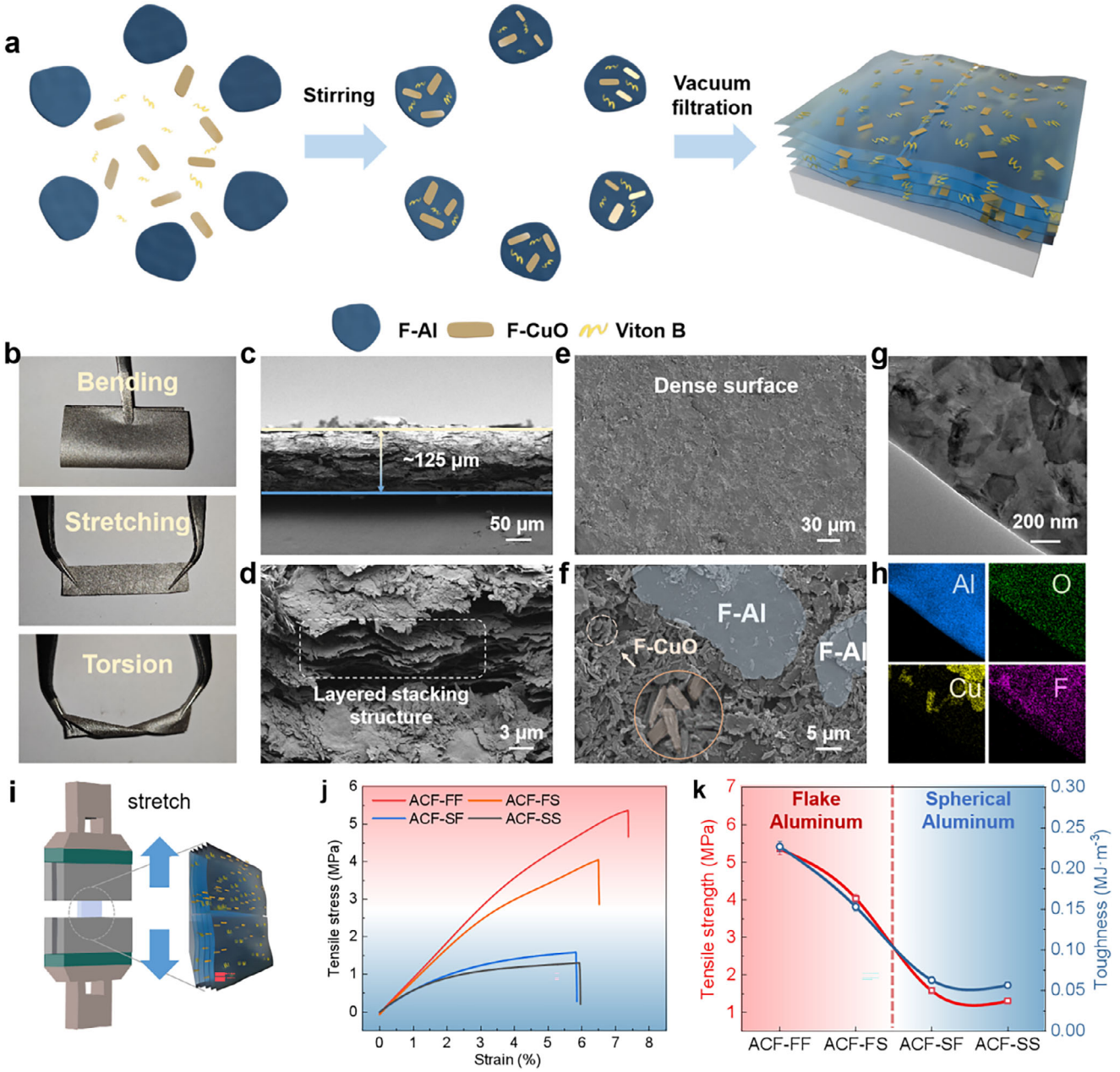

Figure 2. Construction and characterization of nacre-like energetic films. a) Self-assembly process of the composite energetic system with a "brick-and-mortar" layered structure. b) Digital photos show that the films can be bent, stretched and twisted, showing favorable flexibility. c,d) cross-section and e,f) surface SEM images of the energetic films. g,h) HRTEM images and EDS analysis of each component in the films. i) Mechanical properties measurement method, j) tensile stress–strain curve and k) tensile strength and toughness of energetic films.

sliding during deformation. The superior strength (↑156%–308%) and toughness (↑142%–302%) of F-Al-containing systems (ACF-FF/FS) over spherical counterparts (ACF-SF/SS) confirm that F-Al is the primary contributor to enhanced interlayer friction.

The incorporation of F-CuO is not merely a compositional change but a critical structural enhancement that amplifies both mechanical resilience and energy release via geometric synergy. Mechanically, the planar geometry of F-CuO significantly reinforces the nacre-mimetic architecture. Quantitative analysis reveals that the full-2D system (ACF-FF) achieves a 32.4% increase in tensile strength and 48.4% increase in toughness compared to the mixed-dimensional system (ACF-FS). In stark contrast, replacing S-CuO (spherical CuO) with F-CuO in spherical aluminum systems (ACF-SF vs. ACF-SS) yields only marginal gains (20.6% strength/11.1% toughness), underscoring that the strengthening effect is maximized only when F-CuO is geometrically matched with F-Al.

In-situ tensile testing (Figure S7, Supporting Information) elucidates the origin of this enhancement. As stress is applied, the

initial crack does not propagate linearly. Instead, it undergoes significant deflection and bifurcation along the "brick-and-mortar" interfaces, extending the propagation path. Fracture surface analysis further reveals a characteristic "fish-scale" step-like morphology, where F-Al and F-CuO platelets are pulled out with visible filamentous polymer bridging. This indicates that the large contact area of F-CuO facilitates intense interfacial friction and viscoelastic deformation of the binder during interlayer sliding, thereby dissipating substantial energy and preventing catastrophic failure.

To contextualize these mechanical gains, we compared the ACF-FF system with state-of-the-art 3D-printed energetic materials. While additive manufacturing enables complex geometries, high-loading nanothermites and composite propellants often struggle with brittleness or limited tensile strength due to weak interfacial bonding and porosity.[40–43] In contrast, nacre-mimetic film achieves a significantly higher tensile strength of 5.35 MPa and favorable toughness (0.227 MJ m^{-3}). This advantage stems directly from the "brick-and-mortar" architecture, where the ordered arrangement of 2D F-Al and F-CuO platelets promotes crack deflection and frictional energy dissipation. This suggests that the geometric-interfacial regulation in 2D-MICs effectively resolves the trade-off between high solid loading and mechanical robustness.

2.2. Stimulus-Specific Response

According to the classical melt-diffusion theory, the fracture of the protective Al_2O_3 shell constitutes the critical first step for subsequent redox reactions between exposed molten aluminum cores and oxidizers.[44,45] This failure threshold directly dictates the thermal sensitivity and ignition characteristics of aluminum-based energetic systems. Although it has been extensively studied in conventional spherical aluminum, the response of Al_2O_3 shells encapsulating 2D F-Al to transient thermal stress remains under-investigated. Understanding these morphology-dependent mechanical responses is crucial for elucidating the thermal sensitivity of 2D MIC systems.

Thus, finite element analysis was employed to investigate the stress evolution in the Al_2O_3 shell under thermal shock. Transient stress evolution within the Al_2O_3 shell of spherical (S-Al) and flake (F-Al) Al@Al_2O_3 core-shell structures (Figures S2 and S3, Supporting Information) was simulated under identical thermal shock conditions using ANSYS. **Figure 3a** presents time-resolved stress contour plots for both configurations. The S-Al system exhibited uniform stress distribution across its Al_2O_3 shell, with minimal stress gradients observed along the thickness direction. In stark contrast, F-Al displayed pronounced stress localization, where peak stresses concentrated at geometric edges.

Analysis of surface-specific stress profiles (Figure 3b) revealed that both the basal surface (S_b) and lateral surface (S_l) of F-Al sustained maximum stresses significantly exceeding mean values. At the thermal shock peak (t = 1 s), peak stresses on these surfaces surpassed the spatial average by 29%–31%, confirming intense local stress intensification. Combined with stress contours, this demonstrates circumferential edge concentration in F-Al (Figure 3c). This amplified edge stress concentration originates from geometric discontinuities inherent to high-aspect-ratio planar structures. When thermal loads traverse such discontinuities, internal force transfer paths are compelled to divert around abrupt curvature transitions, thereby elevating local stresses through geometric reinforcement effects.[46–48] Conversely, S-Al exhibited near-identical maximum and average stresses on both its inner (S_i) and outer (S_o) shell surfaces (Figure 3d), reflecting homogeneous stress distribution. This uniformity stems from spherical symmetry—continuous curvature eliminates geometric singularities, enabling isotropic dissipation of thermal stresses without local intensification. Critically, these uniform stress values in S-Al remained consistently below the peak edge stresses of F-Al. The intensified edge stress in F-Al substantially reduces the effective fracture strength of the Al_2O_3 shell under thermal excitation. Compared to S-Al, this localized weakening promotes preferential crack initiation at lower global energy inputs. Consequently, reactive molten aluminum cores become more readily exposed during combustion in F-Al systems.

Complementing the simulation analysis, thermal response sensitivity was experimentally quantified through Ni-Cr wire ignition tests (experimental schematic in Figure 3e). Ignition delay was determined by measuring the temporal offset between voltage initiation and photodiode detection signals during combustion (Figure 3f). Experimental results (Figure 3g) demonstrate that 2D energetic systems incorporating F-Al (ACF-FF/FS) exhibit significantly enhanced thermal responsiveness. Their average ignition delays measured 138 and 154 ms, respectively—representing a 42%–50% reduction compared to S-Al systems (ACF-SF: 266 ms; ACF-SS: 275 ms). This pronounced decrease confirms that the 2D hierarchical architecture effectively lowers the thermal excitation threshold of the system.

Collectively, the finite element simulations and ignition experiments demonstrate that the distinct thermal response characteristics of 2D MICs originate from morphology-dependent stress modulation. The geometric discontinuity in F-Al induces localized stress amplification at edges (29%–31% above mean stress), which significantly weakens the Al_2O_3 shell's fracture resistance under thermal excitation. It is worth noting that the thickness fluctuation of the F-Al shell acts as a critical geometric sensitizer for thermal response. Similar to the enhanced reactivity observed in aged aluminum nanostructures,[49] the non-uniform oxide thickness exacerbates localized stress concentration under thermal shock. Thinner or rougher regions of the shell function as preferential failure sites, facilitating early rupture and core exposure. This mechanism will be instrumental in reducing the thermal ignition threshold.

Electrostatic discharge (ESD) poses critical safety risks during the manufacturing, storage, and handling of energetic materials, where accidental ignition may cause catastrophic failure.[50–52] The nacre-inspired layered architecture fundamentally modulates ESD response by establishing continuous conductive pathways. We quantitatively evaluated electrostatic ignition thresholds using a standardized ESD sensitivity apparatus (**Figure 4a,b**) implementing the Bruceton up-down method,[53,54] with 50% ignition energy (E_{50}) as the primary metric.

Results demonstrate that the ACF-FF system exhibits a significantly elevated E_{50} value of 247 mJ, representing a 73% increase compared to the ACF-SS system (E_{50} = 142 mJ), as shown in Figure 4c. Notably, both F-Al-containing systems (ACF-FF/FS) display higher ESD thresholds than their S-Al counterparts,

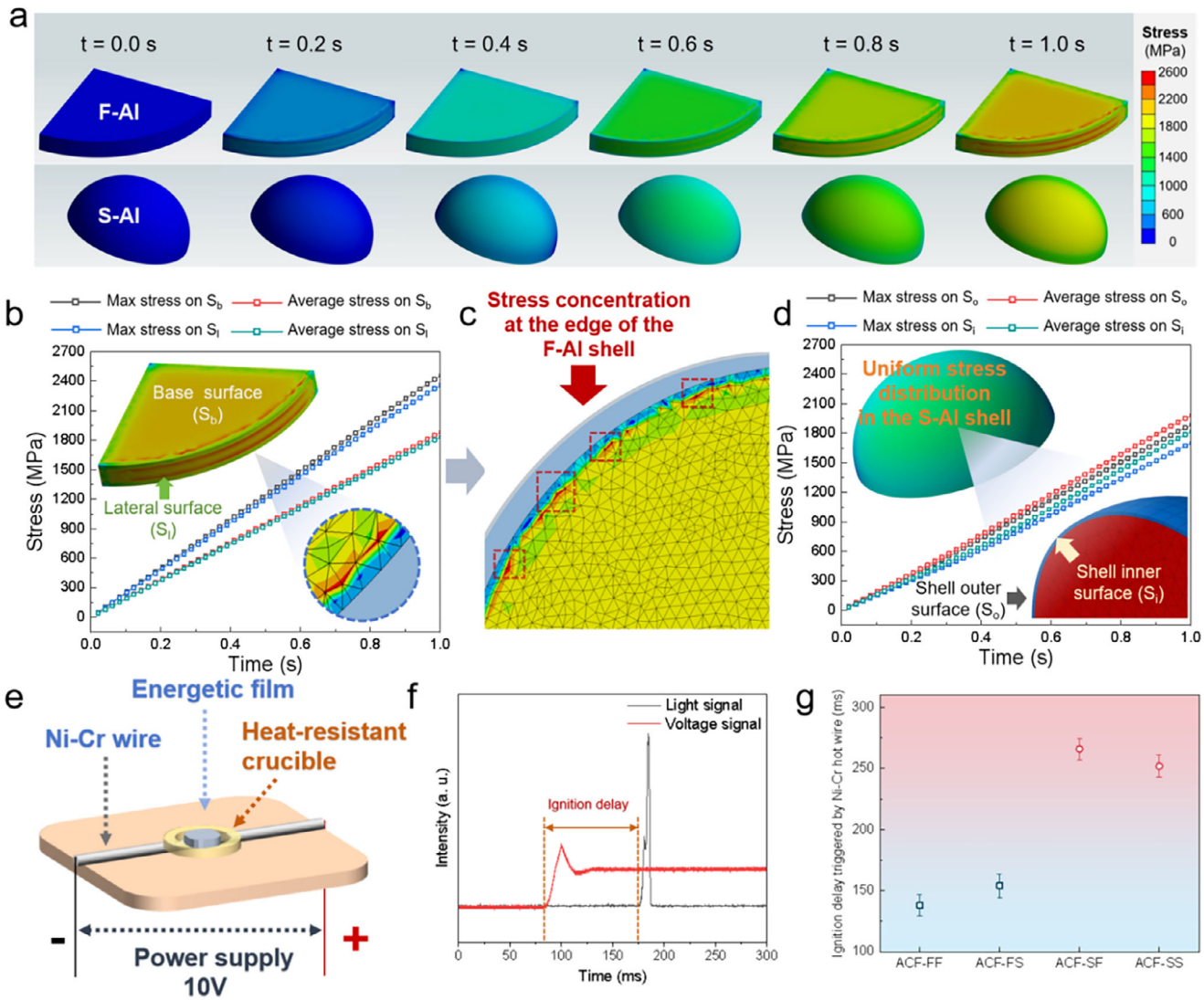

Figure 3. Numerical simulation and experimental measurement of thermal response in energetic systems. a) Thermal stress contours and b–d) stress-time profiles at representative interfaces from finite element simulations of F-Al and S-Al. e,f) Schematic and methodology for Ni-Cr wire ignition delay measurement. g) Ignition delays of various samples under thermal stimulus.

confirming that the 2D morphology of the metallic fuel component is pivotal for enhancing electrostatic safety.

This enhancement stems from fundamentally distinct charge transport characteristics. Conductivity measurements (Figure 4d) reveal that F-Al systems (ACF-FF/FS: 128–1080 mS m^{-1}) exhibit conductivity values 3–4 orders of magnitude higher than their spherical counterparts (ACF-SS/SF: 0.26–0.49 mS m^{-1}). S-Al form discontinuous networks through stochastic point contacts with limited interfacial connectivity and tortuous electron pathways (Figure 4e). This structural discontinuity impedes charge transport, promoting localized electrostatic accumulation under external stimuli that compromises ESD safety. Conversely, the oriented alignment of F-Al establishes percolating in-plane conductive networks that facilitate efficient charge dissipation (Figure 4e), significantly enhancing electrostatic ignition resistance.

2.3. Flame Propagation Characteristics

To elucidate the regulatory mechanism of the nacre-like layered architecture on the combustion behavior of the thermite composites, the self-sustained combustion process of strip-shaped energetic films was quantitatively characterized using an open combustion test platform (**Figure** 5a,b). Analysis of the relationship between the flame front position and time revealed a significant linear correlation for all systems ($R^2 > 0.9$), confirming the stability of the combustion process (Figure 5c). The flame propagation rate (V_u) was calculated from the slope of the linear regression.

Systems utilizing F-Al (ACF-FF and ACF-FS) exhibited propagation rates of 128 and 79 mm s^{-1} respectively, representing a 5–8 fold enhancement over S-Al systems (ACF-SF: 15.9 mm s^{-1}; ACF-SS: 15.1 mm s^{-1}), as shown in Figure 5d. This substantial improvement is primarily attributed to thermally conductive properties arising from the structural design. The

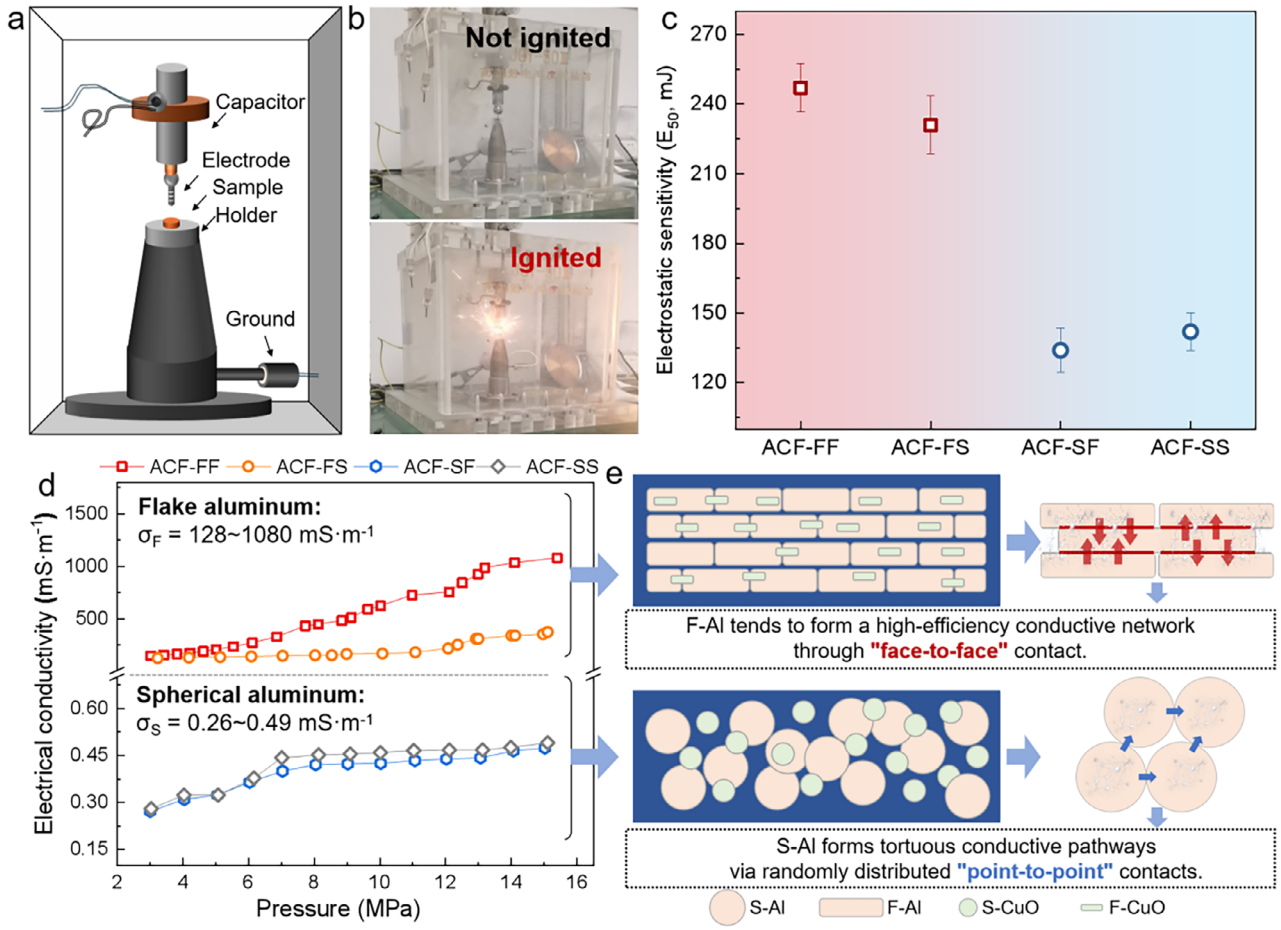

Figure 4. Electric spark sensitivity analysis of energetic films. a,b) Schematic diagram and digital image of electric spark sensitivity measurement device. c) Spark sensitivity and d) conductivity of each sample. e) Relationship between contact characteristics and conductivity of components in a system containing F-Al/S-Al powder.

ACF-FF system exhibits a 62.0% higher burning rate than ACF-FS, whereas the transition from S-CuO to F-CuO in spherical systems (ACF-SF vs. ACF-SS) results in a negligible 5.3% increase. This disparity also originates from the high-efficiency combustion facilitated by the formation of continuous 'face-to-face' contact interfaces between F-Al and F-CuO. Unlike the limited "point-to-point" contacts in spherical mixtures, this 2D topology minimizes interfacial thermal resistance and drastically shortens diffusion distances for oxygen and aluminum ions, synchronizing robust mechanical integrity with accelerated energy release.

Substantiating this analysis, steady-state thermography measurements[31] (**Figure** 6a,b) confirmed significantly enhanced thermal conductivity in F-Al systems. Temperature evolution profiles 10 mm from the heating source (Figure 6c) showed steeper thermal gradients and higher peak temperatures in ACF-FF/FS versus isotropic spherical systems. Quantitative thermal conductivity measurements (Figure 6c) revealed a 186% enhancement in ACF-FF relative to ACF-SS.

This significant enhancement is attributed to the establishment of low-thermal-resistance pathways through the mutual stacking of flake components within the plane[55] (Figure 6d). Critically, the dominant role of aluminum's intrinsically high thermal conductivity (237 W m^{-1} K^{-1}) versus copper oxide (18–40 W m^{-1} K^{-1}) renders the 2D arrangement of F-Al the primary determinant of system-wide thermal transport. Rapid lateral heat conduction accelerates preheating of the unreacted region ahead of the flame front, thereby increasing the flame propagation rate (Figure 6d).

High-speed imaging provided direct evidence of this mechanism. The F-Al composite exhibits a nearly vertical flame front ($\theta \approx 85°$; Figures 5b and 6e), indicating that the combustion front is closer to the in-plane direction ($\lambda_P \gg \lambda_H$). This phenomenon stems from the nacre-like structure, which imparts a much higher thermal conductivity enhancement in the in-plane direction than in the thickness direction ($V_P \gg V_H$).[56] The combustion wave is more easily propagated in the in-plane direction of the film. In contrast, randomly packed spherical particle systems (ACF-SF/SS) lack preferential heat-transfer pathways, promoting relatively uniform heat diffusion in 3D space. Consequently, these systems display smaller flame inclination angles ($\theta \approx 45°$) with distinct curvature observable at the combustion front (Figure 6e), hindering efficient planar self-sustaining propagation.

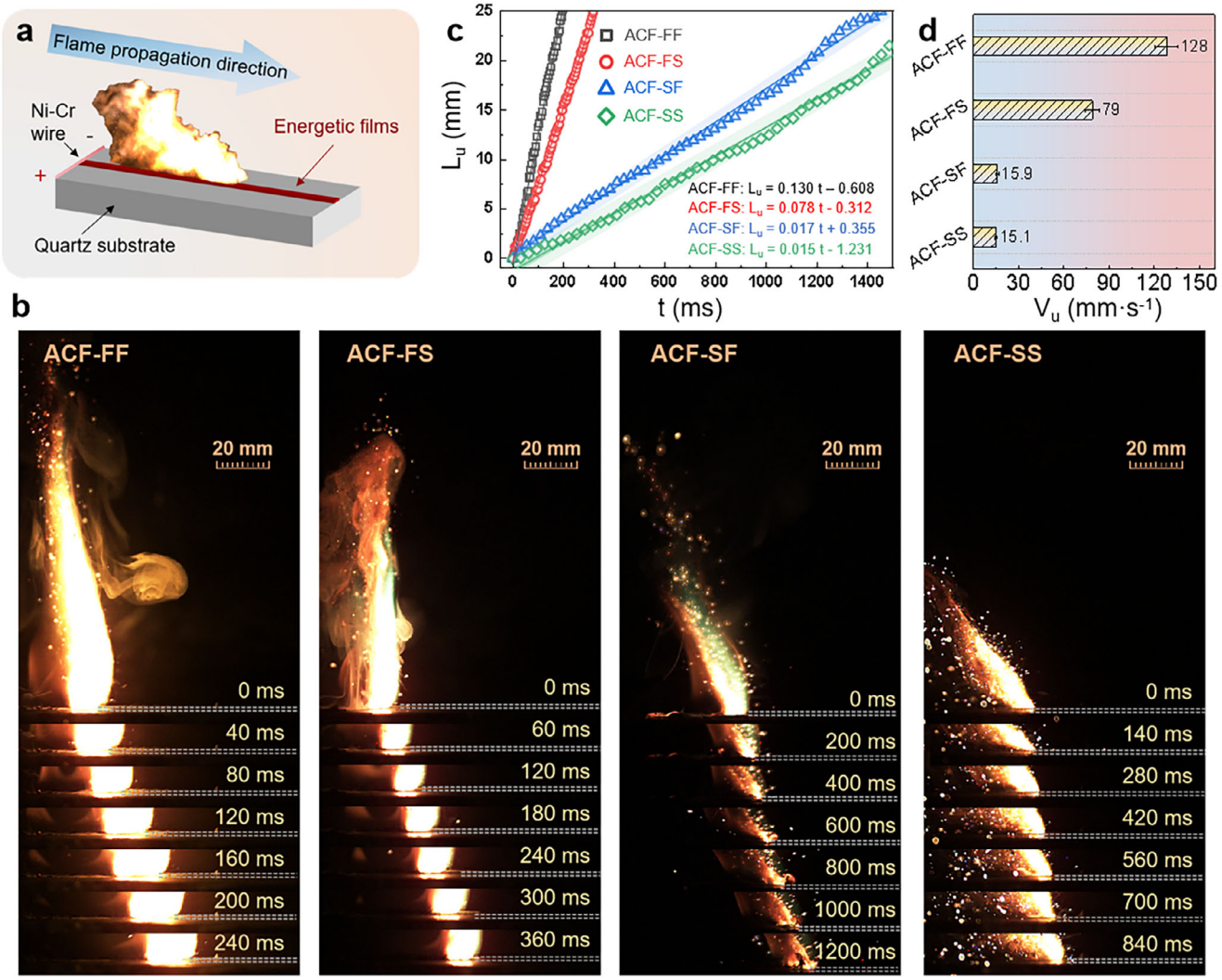

Figure 5. Analysis of flame propagation characteristics. a) Schematic diagram of flame propagation experimental measurement. b) High-speed photography images of flame propagation of each sample. c) Flame propagation front-time curve. d) Flame propagation rate of each system.

Notably, within the 2D F-Al framework, the morphology of CuO significantly influences combustion performance. The propagation rate of ACF-FF (128 mm s^{-1}) exceeds that of ACF-FS (79 mm s^{-1}) by 63%. This difference stems from the unique "2D/2D" contact configuration formed between F-CuO and F-Al, which maximizes interfacial contact area, significantly reduces the solid-solid reaction diffusion barrier. Conversely, in S-Al systems (ACF-SF versus ACF-SS), the difference in propagation rates is merely 5.3% (15.9 vs. 15.1 mm s^{-1}) regardless of oxidizer morphology. This indicates that when the Al is isotropically and randomly distributed, the regulatory effect of oxidizer morphology on reaction kinetics is substantially weakened, and system performance becomes primarily constrained by the discrete.

2.4. Combustion Flame and Condensed Phase Residue

To quantitatively characterize combustion behavior, an analysis was performed by assessing the flame area and the number of incandescent particles. **Figure** 7a illustrates the image processing workflow. High-speed RGB frames were binarized, with the largest connected region designating the flame area and discrete regions representing hot particles.[57] Temporal evolution of these parameters was extracted from sequential image analysis.

Flame area (Figure 7b) and particle count profiles (Figure 7c) reveal distinct combustion signatures. Statistical analysis (Figure 7d) demonstrates that F-Al-dominated systems (ACF-FF: 1007 mm^2; ACF-FS: 398 mm^2) exhibit 3.7 to 5.2 times larger average flame areas during stable combustion than S-Al counterparts (ACF-SF: 213 mm^2; ACF-SS: 192 mm^2). Conversely, incandescent particle density inversely correlates with flame area, showing higher counts in S-Al systems.

Residue morphology and elemental distribution (Figure 7e–j) further corroborate these behavioral differences. S-Al systems (ACF-SF/SS) yield coarser residues (Figure 7g,h) featuring hollow/fragmented Al_2O_3 shells (Figure 7j), consistent with classical melt-diffusion mechanisms where molten Al penetrates the oxide layer, leaving unreactive hollow spheres.

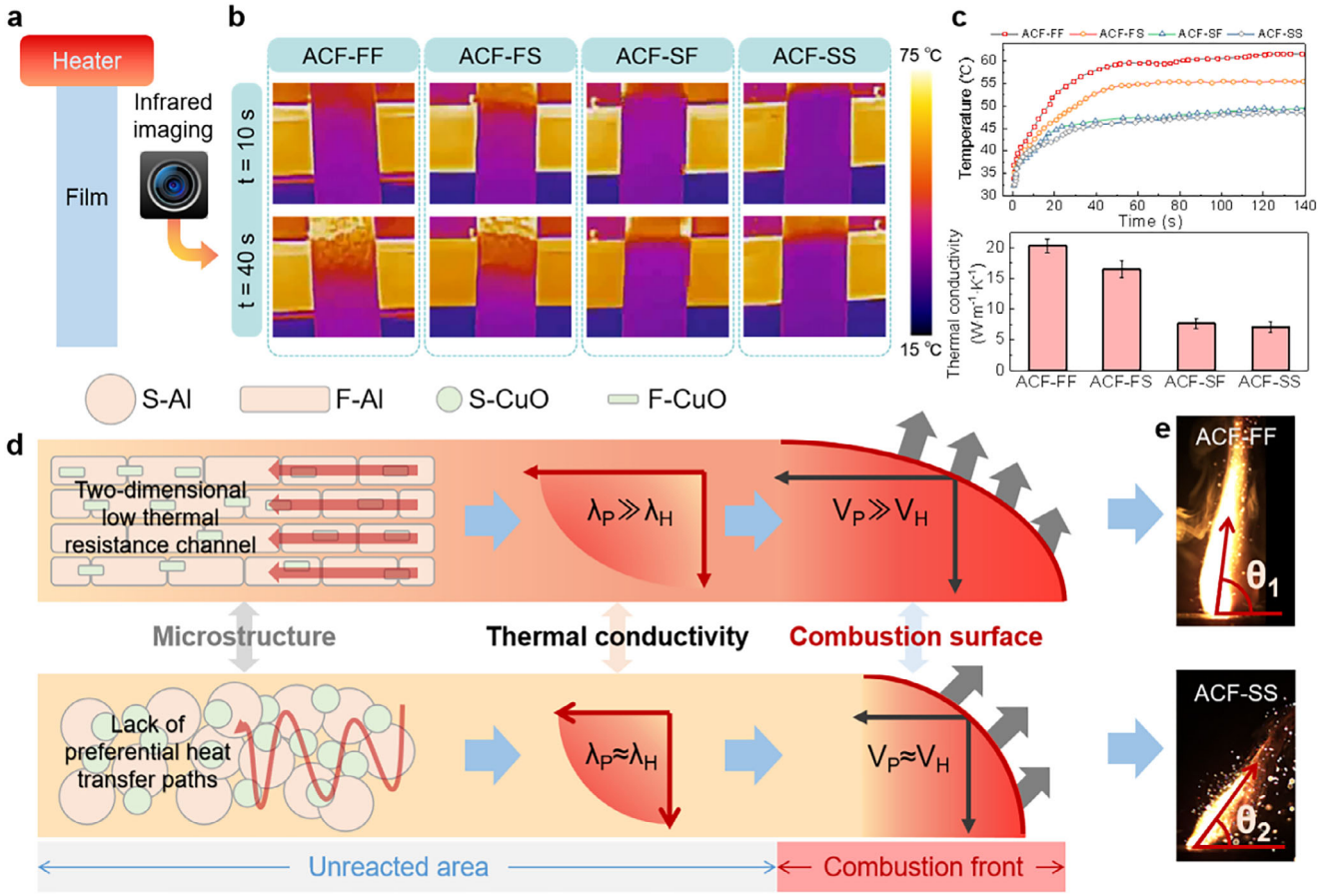

Figure 6. Thermal conductivity and flame propagation morphology analysis of energetic films. a,b) Experimental setup and representative image for thermal conductivity measurement. c) Temperature-time curves and measured thermal conductivity of samples. d) Influence of thermal conductivity differences on flame front morphology and propagation behavior. e) Flame inclination angles of ACF-FF and ACF-SS during combustion.

In contrast, F-Al systems (ACF-FF/FS) produce finer residues containing dense Al/Cu/F-rich spherical agglomerates (Figure 7i), This confirms that despite initial 2D morphology, F-Al undergoes melting and phase transition during combustion, ultimately forming spherical condensed-phase products.[58] This agglomeration behavior fundamentally impacts reaction efficiency. Molten S- Al coalesces rapidly into large droplets through low-barrier collisions,[59,60] sharply reducing specific surface area and hindering oxidation.

F-Al resists immediate spheroidization due to geometric constraints. Instead, it undergoes multistage morphological evolution. Combined with the research of Wang et al.,[58] it is speculated that, the high-aspect-ratio molten aluminum cores preferentially undergo microjet ejection rather than direct spheroidization. These ejected droplets subsequently coalesce into smaller spheres than those formed in S-Al systems. This complex kinetic process prolongs the high-specific-surface-area state of aluminum, extending its reaction window. The resultant spatial and temporal conditions promote efficient oxidation, ultimately manifesting as expanded flame areas and reduced agglomerate sizes in F-Al systems.

2.5. Thermal Reaction Pathway

The thermal reaction pathway of the Al/CuO/fluororubber ternary system has been preliminarily elucidated in prior studies.[61] It is characterized by the fluororubber preferentially undergoing a PIR and Al-F exothermic reaction with aluminum, subsequently triggering the main redox reaction between Al and CuO. The coordinated analysis of DSC (Differential scanning calorimetry) and X-ray photoelectron spectroscopy (XPS) not only confirmed the above-mentioned multi-stage reaction characteristics, but also revealed the significant regulatory effect of aluminum two-dimensionalization on the reaction path.

All samples exhibit three characteristic exothermic peaks in their DSC curves (**Figure** 8a), located at 330–460, 500, and 600 °C, respectively. To elucidate the chemical processes corresponding to each peak, intermediate products at different temperatures were analyzed by XPS. The Al 2p spectrum at 460 °C (Figure 8b) shows characteristic peaks at binding energies of ≈71.9 eV (Al-Al metallic bond) and ≈78.2 eV (Al-F bond).[62] This indicates that Peak 1 primarily originates from the PIR between the Al_2O_3 shell and fluororubber.[63,64] At 500 °C, the Al-Al peak disappears in the Al 2p spectrum (Figure 8c), while the Al-F peak

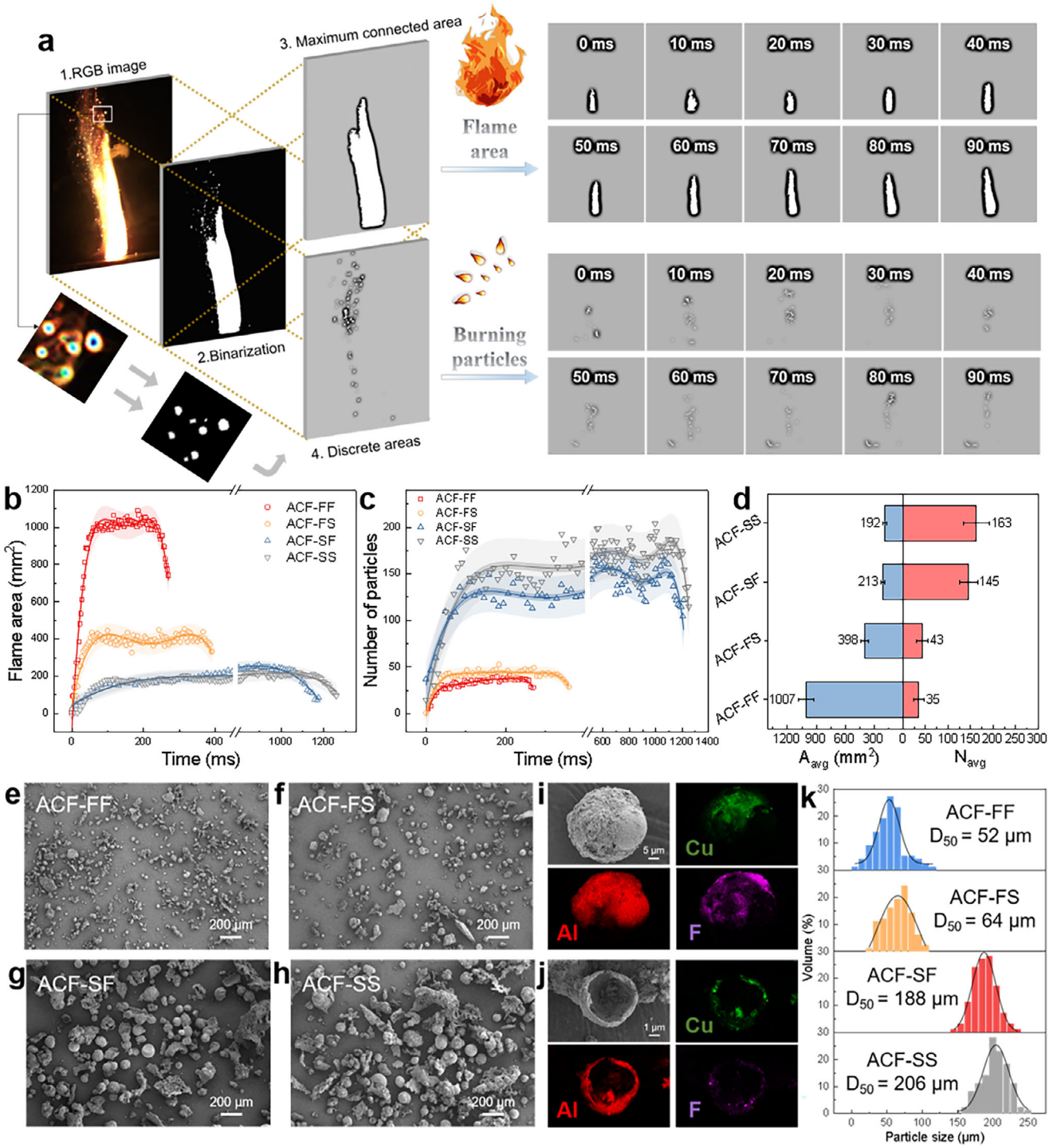

Figure 7. Combustion characterization and condensed-phase residue analysis. a) Representative image processing workflow for flame/particle analysis. b) Flame area versus time profiles and c) particle count versus time profiles for all samples. d) Average flame area and particle count during combustion. Condensed-phase residues: e–h) SEM images, i,j) local EDS mapping, and k) particle size distribution.

intensity significantly increases (Figure 8d), confirming that intense Al-F reactions between the aluminum core and fluororubber occur at this stage, leading to the initial consumption of metallic aluminum. At 600 °C, the Al-O peak becomes dominant (Figure 8d), indicating the system enters the main redox reaction stage between Al and CuO, releasing the primary energy.

Although the reaction stages are similar, the morphology of the aluminum significantly alters the extent and kinetics of each stage. By quantifying the XPS peak area ratio of Al-F to Al-O

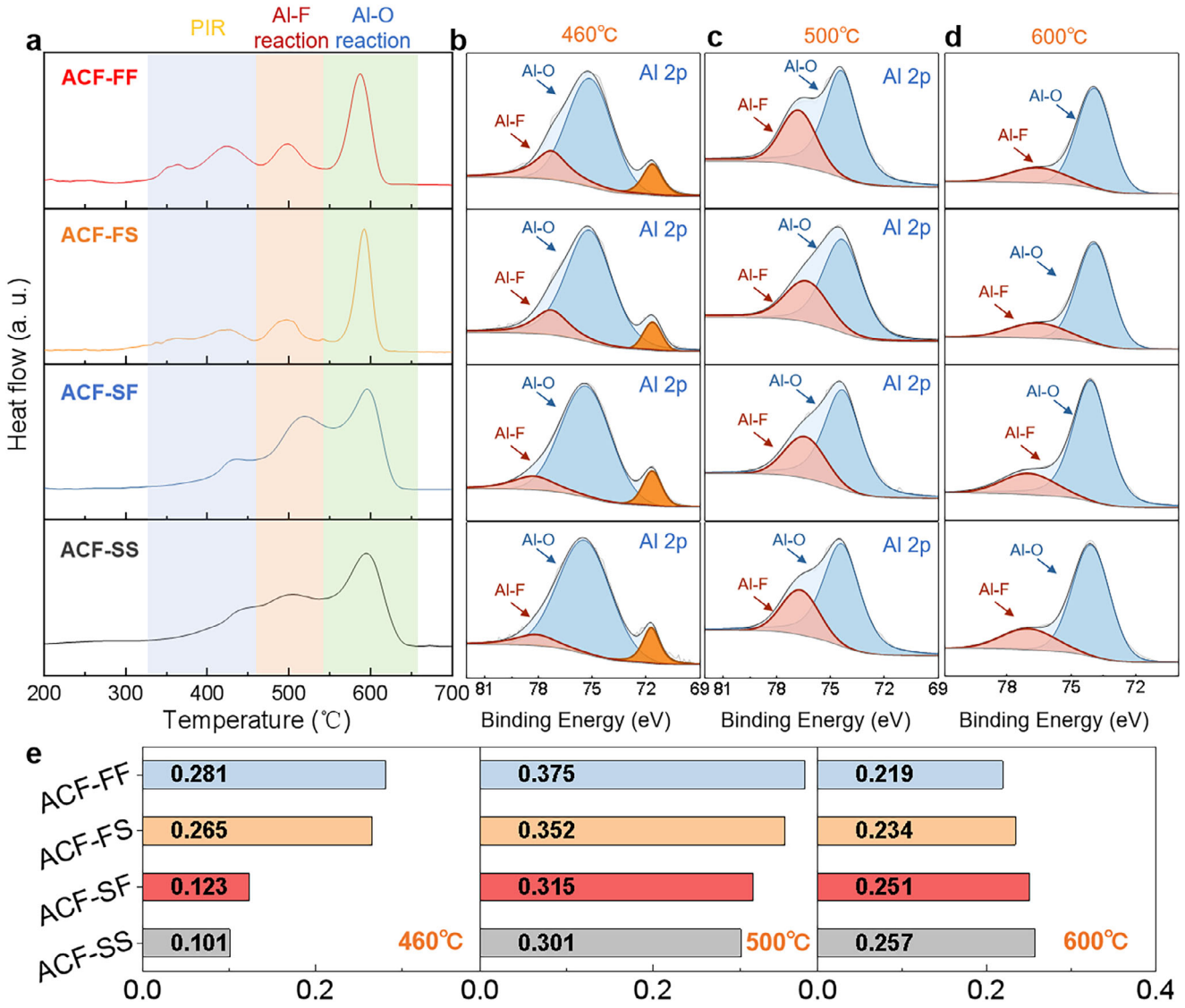

Figure 8. Thermal reaction pathway analysis. a) DSC curve. b–d) XPS high-resolution spectra of Al 2p in the reaction intermediate state at different temperatures. e) Al-F/Al-O peak area ratio in XPS high-resolution spectra at different temperatures.

bonds (Al-F/Al-O), it was found that during the PIR stage (460 °C), the F-Al systems (ACF-FF: 0.281; ACF-FS: 0.265) exhibit significantly higher Al-F/Al-O ratios than the spherical systems (ACF-SF: 0.123; ACF-SS: 0.101). This is attributed to the non-uniform Al_2O_3 shell on F-Al, which is more susceptible to erosion by fluororubber, accelerating the PIR process. The morphological roughness and thickness variations of F-Al significantly enhance interfacial chemical kinetics. The defective, uneven oxide shell created by milling is more susceptible to erosion by the fluoropolymer binder compared to the smooth S-Al surface. This structural feature reduces the diffusion barrier for fluorine species, promoting a more vigorous Al-F reaction. In the main stage of the Al-O reaction (600 °C), the Al-F/Al-O ratio of the flake system is slightly lower than that of the spherical system, indicating that the reaction between Al and CuO is more complete. The Al-O reaction in the system is more complete because the F-Al reacts more fully with PIR and Al-F at the beginning of the reaction, and the corrosion of the surface passivation layer is more obvious. At the same time, the 2D stacking structure improves the contact efficiency of the Al/CuO interface and promotes the complete redox reaction.

2.6. Synergistic Mechanism of 2D-MICs

The nacre-mimetic structure with 2D architecture proposed in this study achieves synergistic and intelligent regulation of the energy release mode, stimulus-response behavior, reaction pathway, and mechanical properties of MICs by reconstructing the spatial arrangement and interfacial characteristics of the fuel and oxidizer (**Figure 9**). Its core lies in the unique physicochemical mechanisms derived from the ordered stacking of 2D lamellar units.

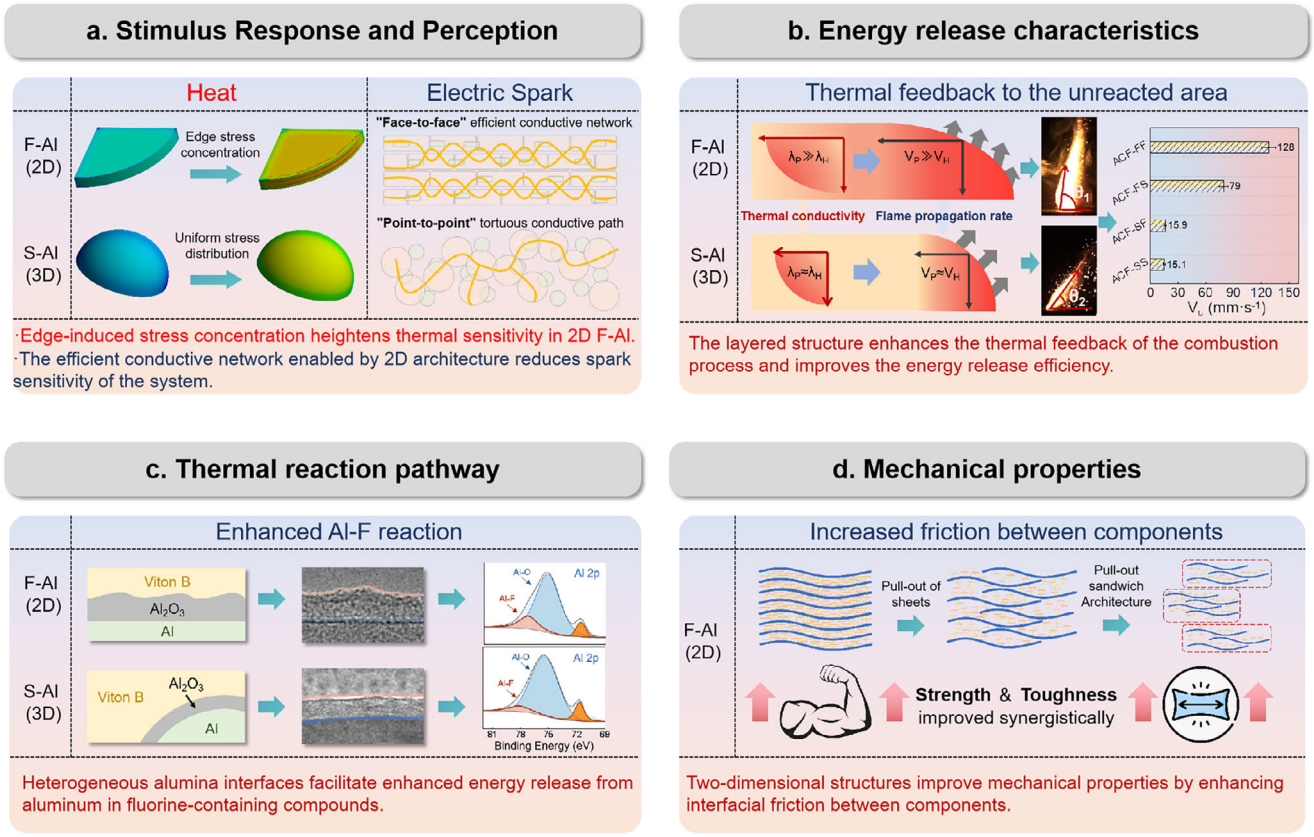

Figure 9. Synergistic mechanism of 2D-MICs: stimulus-specific response, energy release, interface activation and toughening.

In terms of stimulus-response properties, the 2D architecture provides the energetic system with sensitivity selectivity. Regarding the thermal stimulus response, the geometric inhomogeneity of F-Al and the inhomogeneous distribution of the Al_2O_3 shell on its surface lead to obvious local stress concentration in the edge region of the sheet under thermal excitation. This stress concentration significantly weakens the mechanical stability of the Al_2O_3 shell, promoting its preferential rupture at lower thermal excitation energy, thereby exposing the highly reactive Al core. Consequently, the thermal excitation threshold of the system is substantially reduced (Figure 9a).

Regarding the electrostatic spark stimulus response, the continuous 3D conductive network formed by F-Al within the layers provides an efficient migration channel for electrostatic charges. This network significantly enhances the overall electrical conductivity of the material, making it difficult for electrostatic charges to accumulate locally and form high potential differences. Thereby, the electrostatic sensitivity (ESD) of the system is significantly enhanced (ESD_{50} > 247 mJ), improving safety during operation and in specialized application environments (Figure 9a).

In terms of energy output, the 2D layered structure exhibits ultra-high thermal conductivity in the direction parallel to the layer (in-plane), far exceeding the traditional randomly arranged spherical particle system. During combustion, this property drives the rapid lateral diffusion of heat along the lamellae toward the combustion front, forming an "in-plane dominated" flame propagation mode (Figure 9b) (flame inclination angle increased from ≈45° to ≈85°). The high in-plane thermal conductivity establishes an efficient thermal feedback loop between the combustion zone and the unreacted zone. The heat released by combustion is rapidly transferred to adjacent unreacted layers, thereby greatly enhancing the energy release rate (burning rate increased from 15.1 m s^{-1} to at least 128 m s^{-1}).

In terms of chemical reaction patterns, due to the large specific surface area of 2D flake aluminum powder, its surface Al_2O_3 shell exhibits higher chemical heterogeneity. This nonuniformity makes it more susceptible to etching by active fluorine species in the fluoropolymer binder (Figure 9c). This etching thereby weakens the Al_2O_3 shell, facilitating the subsequent Al/CuO redox reaction. The face-to-face contact mode between F-Al and F-CuO (distinct from point contact in sphere-sphere systems) creates a larger effective reaction interface area and shorter diffusion distances. The ordered interlayer arrangement further ensures intimate contact between reactants at the nano/micro scale, providing an ideal platform for efficient and controllable redox reactions.

In terms of mechanical properties, the bionic nacre structure exhibits synergistic toughening and strengthening effects. The 2D lamellae (Al and CuO) undergo relative sliding under stress, generating significant interlayer friction forces. This friction is a key mechanism for dissipating external mechanical energy and hindering crack propagation (Figure 9d). Pulling out flake Al or CuO from the matrix requires overcoming interfacial adhesion

and friction forces, consuming substantial energy. The synergistic action of these mechanisms enables the 2D-MICs to achieve simultaneous enhancement in strength and toughness (tensile strength increased by 308%, toughness increased by 302%) while maintaining high stiffness, significantly improving the material's structural integrity and service reliability under complex loading environments.

In summary, the 2D construction successfully overcomes the mutually exclusive bottleneck between mechanical properties and sensitivity/energy characteristics in traditional MICs by precisely regulating the material's physical structure (conductive/thermal networks, stress distribution), chemical interfaces (Al_2O_3 activation, reaction contact area), and mechanical load transfer paths (interlayer friction, toughening mechanisms). The fundamental rationale for selecting the nacre-structure over other biomimetic models lies in its optimization of interfacial transport and response selectivity. In thermite reactions, reaction rates are governed by heat and mass transfer; the nacre-like "face-to-face" alignment creates continuous 2D interfaces that minimize thermal resistance and shorten diffusion paths significantly more effectively than isotropic or fibrous networks. Furthermore, this specific 2D topology enables a synergistic "stimulus-selective" mechanism: the in-plane conductive network efficiently dissipates electrostatic discharge (enhancing safety), while the edge-induced stress concentrations of the flake components lower the thermal ignition threshold. Thus, the nacre architecture provides a tailored solution to the "safety-energy-mechanics" trade-off that is specific to energetic composites.

3. Conclusion

This study resolves the fundamental conflict between mechanical resilience, safety, and energy release in metastable intermolecular composites (MICs) through a bio-inspired geometric-interfacial nanoarchitectonics strategy. By engineering hierarchically ordered films via the oriented assembly of F-Al and F-CuO into a nacre-mimetic "brick-and-mortar" architecture, we achieve a synergistic optimization of traditionally antagonistic properties. Most significantly, this architecture delivers a stimulus-selective response, representing a pivotal scientific innovation. By exploiting geometric stress concentration at F-Al edges, thermal ignition thresholds are reduced by ≈50%; conversely, percolating conductive networks elevate electrostatic safety by 73% (E50 = 247 mJ). This successfully decouples thermal sensitization from electrostatic desensitization, challenging the traditional "high energy–high sensitivity" paradigm. Underpinning this innovation is the indispensable practical foundation of mechanical robustness. Through synergistic crack deflection and frictional dissipation, the optimized system achieves over 300% increases in both tensile strength and toughness compared to spherical counterparts, thereby reconciling structural integrity with energetic content. Simultaneously, the core intrinsic requirement for energy performance is maximized. Anisotropic in-plane thermal conduction accelerates flame propagation 8-fold (129 mm s^{-1}), while fluorine-mediated interface activation ensures complete redox combustion. This study establishes geometric-interfacial nanoarchitectonics as a transformative paradigm for synchronizing traditionally antagonistic properties in energetic materials, providing foundational principles for next-generation smart energetics.

4. Experimental Section

Materials: Spherical aluminum powder (S-Al, D_{50} = 4.8 µm) was purchased from Shanghai Naio New Materials Co., Ltd. Fluoropolymer Viton (fluorine content 66%) was purchased from Chenguang Chemours Fluoromaterials Co., Ltd. Spherical copper oxide (S-CuO, D_{50} = 0.5 µm), copper nitrate trihydrate ($Cu(NO_3)_2{\cdot}3H_2O$, AR), sodium hydroxide (NaOH, AR) and N,N-dimethylformamide (DMF, AR) were all purchased from Sinopharm Chemical Reagent Co., Ltd.

Synthesis of 2D Materials: F-Al was synthesized by the classical mechanical ball milling method.[31,65] S-Al particles were wet-milled in anhydrous ethanol at a rotation speed of 100 rpm and a ball-to-powder mass ratio of 15:1 for 5 h. F-CuO was synthesized via a modified hydrothermal method.[66] Briefly, 1208 mg of $Cu(NO_3)_2{\cdot}3H_2O$ was dissolved in 40 mL of ultrapure water under vigorous magnetic stirring in an ice-water bath (≤4 °C). A 10 mL aqueous solution of 1.2 M NaOH was gradually added via a constant-pressure dropping funnel over 30 min, followed by continuous high-speed stirring (1200 rpm) for 15 min to form a homogeneous precursor suspension. The mixture was transferred into a 100 mL Teflon-lined autoclave and hydrothermally treated at 130 °C for 2 h. After cooling to room temperature, the black precipitate was collected by vacuum filtration, washed three times with ultrapure water and absolute ethanol, and dried at 60 °C under vacuum for 12 h. The detailed characterization of F-CuO are shown in the Figure S1 (Supporting Information).

Fabrication of Energetic Films: Layered energetic composite membranes were prepared by vacuum-assisted filtration. First, 50 mg of Viton B was dissolved in 10 mL of dimethylformamide (DMF) under ultrasonic and mechanical stirring to form a uniform binder solution A. 300 mg of Viton B was dissolved in 10 mL of DMF to form a uniform binder solution B. Subsequently, 500 mg of F-Al and 500 mg of F-CuO (or a mixture of S-Al and S-CuO) were added to solution A and ultrasonically stirred for 6 h to form a suspension. After that, the suspension was poured into a vacuum-assisted filtration system. When the solvent passed through the filter paper, F-Al and F-CuO remained on the top of the filter paper and were aligned in a parallel direction. Then, solution B was infiltrated into the aligned F-Al and F-CuO to fill the gaps and form a dense composite material. The infiltrated sample was then baked in an oven at 80 °C for 12 h to remove DMF, and the composite membrane was peeled off the filter paper and subsequently hot-pressed. The film compositions (Al/CuO/Viton, ACF) are shown in Table S1 (Supporting Information). According to the morphologies of Al and CuO, the films were named: ACF-FF (F-Al/F-CuO), ACF-FS (F-Al/S-CuO), ACF-SF (S-Al/F-CuO), and ACF-SS (S-Al/S-CuO).

Finite Element Simulation: Finite element simulations were performed using ANSYS 2023 R1 software. Quarter-symmetry geometric models of F-Al and S-Al powders were constructed in ANSYS DesignModeler. For S-Al, the oxide shell diameter measured 2.18 µm with an aluminum core radius of 1.98 µm (Figure S2, Supporting Information). The F-Al model featured an oxide shell of 3.23 × 0.157 µm and an aluminum core of 3.03 × 0.137 µm (Figure S3, Supporting Information). Material properties for Al and Al_2O_3 were sourced from the ANSYS standard library (Table S2, Supporting Information), with temperature-dependent elastic moduli exhibiting linear variation as shown in Figure S4 (Supporting Information). Thermal loading was implemented through a sequential coupling methodology: a steady–state thermal analysis initialized the system at 25 °C, followed by a transient thermal analysis applying a 500 °C ambient temperature. In the structural module, fixed constraints were applied to symmetry planes and core surfaces, while bonded contact defined the core-shell interface, with large deformation effects activated. In the structural module, the core–shell interface was defined using a bonded contact, with large deformation effects activated. Meshing underwent nonlinear mechanical optimization to ensure stress solution convergence.

Characterization: XRD patterns of the obtained materials were recorded using a Bruker D8 Advance diffractometer equipped with monochromatic Cu Kα radiation (λ = 0.15 406 nm). SEM images were

acquired using a Quanta FEG 250, and elemental composition was analyzed with an energy-dispersive spectrometer (EDS, Oxford Instruments) attached to the SEM. HRTEM (FEI Tecnai) and SAED were utilized for detailed structural analysis. X-ray photoelectron spectroscopy (XPS) measurements were conducted with a Thermo Scientific ESCALAB 250i using a monochromatic Al Kα X-ray source (1486.6 eV). The chamber pressure was maintained at 10^{-10} mbar, and all binding energies were referenced to the C 1s peak at 284.8 eV. Differential scanning calorimetry (DSC, TGA/DSC 3+, METTLER TOLEDO) was used for thermal analysis, with a heating rate of 20 °C min^{-1} and an Ar flow rate of 30.0 mL min^{-1}. The particle size distribution of the samples was analyzed using a laser particle size analyzer (Mastersizer 2000/3000, Malvern). The electrical conductivity of the composite films was obtained using a four-probe electrical conductivity tester (Runhu, RH-2661). An infrared thermal imager (ImageIR@8355, InfraTec, Germany) was used to measure the temperature distribution of the film under heating conditions. The actual surface temperature of the sample was measured using a contact thermocouple while simultaneously adjusting the emissivity setting of the thermal camera until the radiometric reading matched the thermocouple value. This process was repeated at steady states between 50–100 °C. The thermal conductivity of the films was measured using a thermal conductivity meter (Hot Disk TPS 2500S) using the transient planar heat source method.

Experimental Setup: Ignition of the energetic materials in the experiments was achieved using a Ni-Cr heated wire and a constant voltage DC power supply. The Ni-Cr wire had a diameter of 0.12 mm and a resistance of ≈3 Ω. The ignition and flame propagation processes were recorded with a high-speed camera (Phantom UHS). In the experiments testing open ignition characteristics, the sample was placed in a quartz crucible at the center of the sample stage and ignited from the bottom by a Ni-Cr wire powered by a direct current source (20 V).

Supporting Information

Supporting Information is available from the Wiley Online Library or from the author.

Acknowledgements

This research was supported by the National Natural Science Foundation of China (Grant Nos. 22305100, 22405104), the Hubei Provincial International Science and Technology Cooperation Program Project (Grant No. 2023EHA014), the Ministry of Human Resources and Social Security of the People's Republic of China (Grant Nos. Y20240022, H20240275), the Hubei Natural Science Foundation (Grant No. 2025AFB460), Hubei Province Foreign Experts Program (Grant No. 2025DJC012), the Hubei Provincial Department of Education Scientific Research Project (Grant Nos. F2023033, Q20234414), the Wuhan Natural Science Foundation Exploration Project (Chenguang Program) (Grant No. 2025040601020173), the Wuhan Youth Science and Technology Talent Zhaoyang Support Project (Grant No. 20250911A07) and the Jianghan University Scientific Research Startup Fund (Grant Nos. PBSKL-2024-QD-03, PBSKL-2025-QD-03). The authors extend the sincere gratitude to the following individuals from Al-Farabi Kazakh National University: Meruyert Nazhipkyzy, Zhandos Tauanov, Sabit Tursynbek, Ayagoz Bakkara, and Makpal Seitzhanova. Their invaluable insights were instrumental during the stages of data processing and experimental design.

Conflict of Interest

The authors declare no conflict of interest.

Data Availability Statement

The data that support the findings of this study are available from the corresponding author upon reasonable request.

Keywords

energy performance, geometric-interfacial, mechanical resilience, metastable intermolecular composites, nacre-mimetic, nanoarchitectonics, stimulus-selective

Received: September 29, 2025
Revised: November 20, 2025
Published online: December 12, 2025

[1] W. He, P. J. Liu, G. Q. He, M. Gozin, Q. L. Yan, *Adv. Mater.* **2018**, *30*, 1706293.
[2] L. Gamba, J. A. Lajoie, T. R. Sippel, E. B. Secor, *Adv. Funct. Mater.* **2023**, *33*, 2304060.
[3] R. Xu, Z. Xue, D. Yang, X. Li, H. Nie, Y. Guo, H. Guo, Q.-L. Yan, J. Gu, *Adv. Funct. Mater.* **2025**, *35*, 2423205.
[4] J. Li, X. Liu, Q. Huang, F. Liu, Q. Xie, M. Hu, J. Su, C. Zhang, Y. Zeng, C. Zhu, *Chem. Eng. J.* **2023**, *468*, 143591.
[5] L. Zhang, X. Li, S. Wang, X. Su, M. Zou, *Combust. Flame* **2024**, *260*, 113109.
[6] D. Liu, J. Wang, X. Zhao, Z. Yang, *Adv. Funct. Mater.* **2025**, *35*, 2418301.
[7] S. Wang, Q. Wang, X. Feng, B. Wang, L. Yang, *Adv. Mater.* **2017**, *29*, 1701898.
[8] T. Wu, V. Singh, B. Julien, M. I. Mendoza-Diaz, F. Mesnilgrente, S. Charlot, C. Rossi, *Sens. Actuators, A* **2024**, *376*, 115573.
[9] Y. Zhou, K. Shi, M. Chowdhury, E. Hagen, Y. Wang, M. R. Zachariah, *Fuel* **2025**, *387*, 134348.
[10] J. Xu, J. Zhang, F. Li, S. Liu, Y. Ye, R. Shen, *FirePhysChem* **2024**, *4*, 95.
[11] A. Wang, C. J. MacRobbie, A. Baranovsky, J. P. Hickey, J. Z. Wen, *Carbon* **2024**, *216*, 118596.
[12] H. Wang, J. Shen, D. J. Kline, N. Eckman, N. R. Agrawal, T. Wu, P. Wang, M. R. Zachariah, *Adv. Mater.* **2019**, *31*, 1806575.
[13] V. Goetz, P. Gibot, D. Spitzer, *Chem. Eng. J.* **2022**, *427*, 131611.
[14] J. Wang, Z. Guo, S. Chen, W. Zhang, H. Cui, Z. Qin, K. Xu, *Ceram. Int.* **2022**, *48*, 20825.
[15] R. Steelman, B. Clark, M. L. Pantoya, R. J. Heaps, M. A. Daniels, *J. Electrostat.* **2015**, *76*, 102.
[16] R. Thiruvengadathan, C. Staley, J. M. Geeson, S. Chung, K. E. Raymond, K. Gangopadhyay, S. Gangopadhyay, *Propellants, Explos., Pyrotech.* **2015**, *40*, 729.
[17] Y. Wang, F. Li, Y. Shen, C. A. Wang, Z. Zhang, J. Xu, Y. Ye, R. Shen, *Combust. Flame* **2021**, *233*, 111580.
[18] J. Dai, J. Xu, F. Wang, Y. Tai, Y. Shen, R. Shen, Y. Ye, *Mater. Des.* **2018**, *143*, 93.
[19] Y. Xue, Q. Zhang, W. Wang, H. Cao, Q. Yang, L. Fu, *Adv. Energy Mater.* **2017**, *7*, 1602684.
[20] F. Liu, Z. Fan, *Chem. Soc. Rev.* **2023**, *52*, 1723.
[21] Y. Zhang, C. He, Q. Yu, X. Li, X. Wang, Y. Zhang, J. Wang, C. Jiang, Y. Jia, X.-C. Zhang, B. Sun, R. O. Ritchie, S. T. Tu, *Nat. Commun.* **2024**, *15*, 6917.
[22] S. Gupta, H. S. Esmaeeli, R. Moini, *Adv. Funct. Mater.* **2024**, *34*, 2313516.
[23] S. Wang, L. Tan, Z. Yang, H. Zhao, L. Guo, *Adv. Mater.* **2024**, *36*, 2401883.
[24] W. Wu, Y. He, Q. Zhu, Z. Luo, B. Li, *New J. Chem.* **2025**, *49*, 3128.
[25] K. Gong, Y. Peng, A. Liu, S. Qi, H. Qiu, *Compos. Part A Appl. Sci. Manuf.* **2024**, *176*, 107857.
[26] H. Zhao, S. Liu, Y. Wei, Y. Yue, M. Gao, Y. Li, X. Zeng, X. Deng, N. A. Kotov, L. Jiang, *Science* **2022**, *375*, 551.
[27] M. Yang, N. A. Kotov, *Nat. Rev. Mater.* **2025**, *10*, 382.
[28] S. Kumar, H. Le Ferrand, *J. Am. Ceram. Soc.* **2025**, *108*, 20623.

[29] V. Vilchez, S. Rawson, S. Zhou, J. McGregor, M. Lawson, A. Rack, Y. Chen, P. J. Withers, F. Bouville, *Acta Mater.* **2024**, *280*, 120338.
[30] J. Xiong, X. Zhao, Z. Liu, H. Chen, Q. Yan, H. Lian, X. He, *Nano-Micro Lett.* **2025**, *17*, 1.
[31] Y. Jiang, D. Ka, A. H. Huynh, X. Zheng, *Chem. Eng. J.* **2024**, *502*, 158121.
[32] J. Wang, Y. Mao, G. Li, H. M. Yin, *Chem. Eng. J.* **2022**, *441*, 136014.
[33] J. M. Slocik, L. F. Drummy, M. B. Dickerson, C. A. Crouse, J. E. Spowart, R. R. Naik, *Small* **2015**, *11*, 3539.
[34] J. Wang, H. M. Yin, Y. F. Mao, L. F. Yang, X. Chen, *Energ. Mater. Front.* **2024**, *5*, 141.
[35] S. M. Chen, H. L. Gao, X. H. Sun, Z. Y. Ma, T. Ma, J. Xia, Y.-B. Zhu, R. Zhao, H.-B. Yao, H.-A. Wu, S. H. Yu, *Matter* **2019**, *1*, 412.
[36] M. S. El-Eskandarany, A. Al-Hazza, L. A. Al-Hajji, N. Ali, A. A. Al-Duweesh, M. Banyan, F. Al-Ajmi, *Nanomaterials* **2021**, *11*, 2484.
[37] A. S. Rogachev, N. F. Shkodich, S. G. Vadchenko, F. Baras, D. Y. Kovalev, S. Rouvimov, A. A. Nepapushev, A. S. Mukasyan, *J. Alloys Compd.* **2013**, *577*, 600.
[38] B. Sun, S. Wang, C. Mao, R. Qiao, M. Ravivarma, S. Liu, H. Fan, J. Xie, J. Song, *Angew. Chem., Int. Ed.* **2025**, *64*, 202412867.
[39] Z. B. Zhang, H. L. Gao, S. M. Chen, S. H. Yu, *Adv. Mater.* **2025**, 2506308.
[40] J. Shen, H. Wang, D. J. Kline, Y. Yang, X. Wang, M. Rehwoldt, T. Wu, S. Holdren, M. R. Zachariah, *Combust. Flame* **2020**, *215*, 86.
[41] J. Lajoie, J. Blocker, T. Sippel, *J. Propuls. Power* **2023**, *39*, 936.
[42] A. Zumbo, L. Stumpo, P. Antonaci, A. Ferrero, F. Masseni, G. Polizzi, G. Tetti, D. Pastrone, *Polymers* **2024**, *16*, 576.
[43] F. Bazzal, J. S. Hoffmann, G. Young, M. J. Bortner, C. B. Williams, *ACS Appl. Eng. Mater.* **2025**, *3*, 482.
[44] V. I. Levitas, *Combust. Flame* **2009**, *156*, 543.
[45] V. I. Levitas, M. L. Pantoya, S. Dean, *Combust. Flame* **2014**, *161*, 1668.
[46] T. S. Park, M. Dao, S. Suresh, A. J. Rosakis, D. Pantuso, S. Shankar, *J. Electron. Mater.* **2008**, *37*, 777.
[47] W. D. Pilkey, D. F. Pilkey, Z. Bi, *Peterson's stress concentration factors*, John Wiley & Sons, Hoboken, NJ **2020**.
[48] Y. Zou, R. You, H. Li, D. Zhang, *Therm. Sci. Eng. Prog.* **2024**, *48*, 102420.
[49] T. Wu, G. Lahiner, C. Tenailleau, B. Reig, T. Hungría, A. Estève, C. Rossi, *Chem. Eng. J.* **2021**, *418*, 129432.
[50] C. Wan, Y. Xiong, H. Qin, Z. Qin, S. Chen, K. Xu, *Appl. Surf. Sci.* **2024**, *661*, 160044.
[51] Y. Zhu, S. Dong, Y. Zhang, L. Cui, S. Chen, F. Zhao, K. Xu, *Chem. Eng. J.* **2025**, 163071.
[52] R. Xu, X. Li, Z. Xue, D. Yang, S. Chen, K. Xu, Q.-L. Yan, H. Nie, *Combust. Flame* **2025**, *273*, 113929.
[53] D. Christensen, G. P. Novik, E. Unneberg, *Propellants, Explos., Pyrotech.* **2024**, *49*, 202400022.
[54] L. Zhang, X. Y. Wang, L. Yang, H. Wang, Q. Y. Wang, *Small* **2025**, *21*, 2500341.
[55] H. Yu, L. Peng, C. Chen, M. Qin, W. Feng, *Nano-Micro Lett.* **2024**, *16*, 198.
[56] Y. F. Huang, Z. G. Wang, H. M. Yin, J. Z. Xu, Y. Chen, J. Lei, L. Zhu, F. Gong, Z. M. Li, *ACS Appl. Nano Mater.* **2018**, *1*, 3312.
[57] X. Liu, J. Li, S. Feng, Y. Jia, M. Hu, Y. Yao, J. Sun, Q. Xie, H. Sang, *Adv. Sci.* **2025**, *12*, 2415073.
[58] Q. Jing, D. Wang, Q. Liu, C. Shi, J. Liu, *Chem. Eng. Sci.* **2022**, *252*, 117502.
[59] X. Liao, J. Pei, P. Xie, Y. Hu, J. Liu, *Propellants, Explos., Pyrotech.* **2024**, *49*, 202300131.
[60] Y. Tang, C. Kong, Y. Zong, S. Li, J. Zhuo, Q. Yao, *Proc. Combust. Inst.* **2017**, *36*, 2325.
[61] K. Xiong, Z. Wang, R. Liu, H. Nie, Q. L. Yan, *Langmuir* **2023**, *39*, 13850.
[62] J. Li, X. Liu, Z. Ming, Y. Jia, J. Sun, Y. Yao, Q. Xie, Y. Shen, Z. Zhao, G. Yin, S. Tursynbek, M. Nazhipkyzy, Z. Tauanov, A. Bakkara, M. Seitzhanova, *Defence Technology* **2025**.
[63] X. Zhang, H. Li, X. Cui, W. Fei, X. Ma, J. Liu, P. Li, X. Guo, X. Zhou, *Fuel* **2025**, *382*, 133564.
[64] J. Li, X. Liu, Z. Zhang, Y. Wang, M. Zhang, K. Guo, F. Duanmu, C. Zhu, *J. Alloys Compd.* **2023**, *936*, 168160.
[65] G. Fan, Y. Jiang, Z. Tan, Q. Guo, D. B. Xiong, Y. Su, R. Lin, L. Hu, Z. Li, D. Zhang, *Carbon* **2018**, *130*, 333.
[66] W. Li, L. Li, Q. Xia, S. Hong, L. Wang, Z. Yao, T.-S. Wu, Y.-L. Soo, H. Zhang, T. W. Benedict Lo, A. W. Robertson, Q. Liu, L. Hao, Z. Sun, *Appl. Catal., B Environ.* **2022**, *318*, 121823.